Lawrence Berkeley National Laboratory
LBL Publications

Title
Unlikelihood of a phonon mechanism for the high-temperature superconductivity in La3Ni2O7

Permalink
https://escholarship.org/uc/item/5xg0r8h0

Journal
npj Computational Materials, 11(1)

ISSN
2057-3960

Authors
You, Jing-Yang
Zhu, Zien
Del Ben, Mauro
et al.

Publication Date
2025-12-01

DOI
10.1038/s41524-024-01483-4

Copyright Information
This work is made available under the terms of a Creative Commons Attribution License, available at https://creativecommons.org/licenses/by/4.0/

Peer reviewed

eScholarship.org Powered by the California Digital Library
University of California

npj | computational materials

Article

Published in partnership with the Shanghai Institute of Ceramics of the Chinese Academy of Sciences

https://doi.org/10.1038/s41524-024-01483-4

Unlikelihood of a phonon mechanism for the high-temperature superconductivity in $La_3Ni_2O_7$

Check for updates

Jing-Yang You[1,2], Zien Zhu[2], Mauro Del Ben[3], Wei Chen[1,4] & Zhenglu Li[2]

The discovery of ~80 K superconductivity in nickelate $La_3Ni_2O_7$ under pressure has ignited intense interest. Here, we present a comprehensive first-principles study of the electron-phonon (*e*-ph) coupling in $La_3Ni_2O_7$ and its implications on the observed superconductivity. Our results conclude that the *e*-ph coupling is too weak (with a coupling constant $\lambda \lesssim 0.5$) to account for the high T_c, albeit interesting many-electron correlation effects exist. While Coulomb interactions (via *GW* self-energy and Hubbard *U*) enhance the *e*-ph coupling strength, electron doping (oxygen vacancies) introduces no major changes. Additionally, different structural phases display varying characteristics near the Fermi level, but do not alter the conclusion. The *e*-ph coupling landscape of $La_3Ni_2O_7$ is intrinsically different from that of infinite-layer nickelates. These findings suggest that a phonon-mediated mechanism is unlikely to be responsible for the observed superconductivity in $La_3Ni_2O_7$, pointing instead to an unconventional nature.

The recent discovery of pressure-induced (14.0–43.5 GPa) superconductivity in the Ruddlesden-Popper phase nickelate $La_3Ni_2O_7$[1] has attracted significant research attention due to its high critical temperature $T_c \sim 80$ K. Prior to this discovery, cuprates were the sole known unconventional superconductors exhibiting *bulk* superconductivity with T_c above the boiling point of liquid nitrogen[2–5]. Unlike cuprates, where the Fermi surface is only associated with Cu $d_{x^2-y^2}$ orbitals, the low-energy states of $La_3Ni_2O_7$ feature both Ni $d_{x^2-y^2}$ and d_{z^2} orbitals, and the metallization of the latter upon pressure was proposed as a key factor behind its high-T_c superconductivity[1,6]. Effective models suggested significant intra-orbital exchange within Ni d_{z^2} orbitals, along with inter-orbital hybridization between Ni d_{z^2} and $d_{x^2-y^2}$ orbitals facilitated by O-*p* orbitals, potentially playing a pivotal role in the observed superconductivity[6–13]. Concurrently, extensive research has explored the pairing symmetry[14–16], the influence of Hund's coupling[7,16,17], and the electronic correlation effects in pristine $La_3Ni_2O_7$[18–21]. Despite these efforts, the mechanism for the superconductivity in $La_3Ni_2O_7$ remains elusive and highly debated.

The first discovered nickel-based superconductor is the infinite-layer nickelate[22] $Nd_{1-x}Sr_xNiO_2$, with a highest $T_c \sim 20$ K[23]. In its undoped parent compound, Ni^+ adopts a $3d^9$ valence electron configuration (similar to Cu^{2+} in cuprates). While the nature of superconductivity in infinite-layer nickelates remains under debate, the conventional electron-phonon (*e*-ph) coupling mechanism initially faced skepticism[24–27]. Early density functional theory (DFT) calculations estimated the *e*-ph coupling constant λ in $Nd_{0.8}Sr_{0.2}NiO_2$ to be ~0.2, implying that phonon-mediated T_c would not exceed 1 K, thus supporting the hypothesis of unconventional pairing mechanisms given the analog to cuprates[28]. Yet, recent studies employing full *GW*-level descriptions (of the band energies using *GW* method, and of the *e*-ph matrix elements via *GW* perturbation theory (*GW*PT)[27,29–31]), which incorporate many-electron self-energy effects, predicted that *e*-ph coupling can mediate two-gap *s*-wave superconductivity in $Nd_{1-x}Sr_xNiO_2$[27]. In contrast to Ni d^9 electron configuration of parent infinite-layer nickelates, bulk $La_3Ni_2O_7$ hosts a Ni $d^{7.5}$ configuration and achieves a significantly higher T_c, raising questions about the roles of *e*-ph coupling as well as its connection or distinction with infinite-layer nickelates. Hence, it is both urgent and critical to scrutinize the implications of *e*-ph coupling including the electron correlation effects on the high-T_c superconductivity in $La_3Ni_2O_7$.

In this work, we have systematically studied the electronic structure and *e*-ph coupling properties of $La_3Ni_2O_7$, incorporating correlation effects through *GW*[32–34], *GW*PT[29], and density functional theory (DFT) plus Hubbard *U* (DFT+*U*)[35,36] approaches. The *GW* approximation to the electron self-energy Σ captures long-range correlation effects from Coulomb interactions, whereas DFT+*U* models short-range (onsite) correlations. In

[1]Department of Physics, National University of Singapore, 2 Science Drive 3, Singapore, 117551, Singapore. [2]Mork Family Department of Chemical Engineering and Materials Science, University of Southern California, Los Angeles, CA, 90089, USA. [3]Applied Mathematics and Computational Research Division, Lawrence Berkeley National Laboratory, Berkeley, CA, 94720, USA. [4]Department of Chemistry, National University of Singapore, 3 Science Drive 3, Singapore, 117543, Singapore. e-mail: zhenglul@usc.edu

both frameworks, we find that the *e*-ph coupling is insufficient to mediate superconductivity with a T_c as high as 80 K. We further explore the effects of electron doping (which are induced by oxygen vacancies experimentally) and alternative structural phases, however, the *e*-ph coupling remains weak. Across all scenarios studied, the *e*-ph coupling constant λ stays below 0.5, while a T_c of 80 K may need λ well above 1.0[37–39] in standard phonon-mediated superconductivity scenarios. The consistently weak *e*-ph coupling strength, even when considering Coulomb interactions and various experimental aspects using state-of-the-art ab initio approaches, suggests that *e*-ph coupling (alone) is unlikely to mediate the high-T_c superconductivity in $La_3Ni_2O_7$ under pressure. Our results *indirectly* support an unconventional pairing mechanism.

Results

GW self-energy effects

The structure of $La_3Ni_2O_7$ in the superconducting phase was initially identified as of *Fmmm* space group[1], supported by room-temperature X-ray diffraction (XRD) measurements[1]. However, subsequent in situ low-temperature and high-pressure synchrotron XRD experiments determined that the tetragonal phase with an *I*4/*mmm* space group is the more likely phase hosting the high-T_c superconductivity[40]. These two structures are very similar to each other, with *Fmmm* having a slight (~1%) symmetry breaking between the in-plane lattice vectors (in the conventional cell). The minor structural variation does not fundamentally alter the band structure of $La_3Ni_2O_7$. In this work, we focus on the properties of $La_3Ni_2O_7$ based on the high-symmetry *I*4/*mmm* structure (Fig. 1a) under high pressure (at 30 GPa), unless otherwise stated.

Given the substantial band renormalization and enhanced *e*-ph matrix elements revealed in infinite-layer $Nd_{1-x}Sr_xNiO_2$ due to *GW* self-energy effects[27], it is imperative to thoroughly examine the correlation effects in $La_3Ni_2O_7$. We first compare the band structures from DFT and *GW* calculations, as shown in Fig. 1b and c, respectively. The Ni atoms in $La_3Ni_2O_7$ exhibit a $t_{2g}^6 e_g^{1.5}$ valence electron configuration, with fully occupied t_{2g} orbitals below 0.5 eV of the Fermi energy (E_F) and partially filled e_g orbitals. Notably, the Ni $d_{x^2-y^2}$ band intersects E_F with a bandwidth of over 3 eV. In addition, the d_{z^2} orbitals exhibit both bonding and antibonding states due to the large interplanar coupling between the NiO_2 layers via the hybridization with the apical O 2*p* orbitals. In the DFT band structure, the La $5d_{x^2-y^2}$ orbital lies 0.56 eV above E_F at the *Z* point as shown in Fig. 1b. In Fig. 1c, the *GW* self-energy effects shift the Ni-d_{z^2} bonding state downward, rendering it fully occupied, while pushing the Ni-$d_{x^2-y^2}$ band upward. The bonding-antibonding splitting of the Ni-d_{z^2} orbital is also increased. Moreover, the La $d_{x^2-y^2}$ band shifts significantly downwards towards the E_F, particularly near the Γ and *Z* points in Fig. 1c, following a similar trend to the Nd d_{z^2} states in infinite-layer nickelate $Nd_{1-x}Sr_xNiO_2$ upon self-energy effects[27].

The *GW* self-energy does not alter most states at the E_F in $La_3Ni_2O_7$. On the other hand, there is growing evidence[27,30,31,41–44] that many-electron correlations can renormalize the *e*-ph matrix elements (describing individual scattering events). To examine the impact of electron correlations (through *GW* self-energy) on these matrix elements, we adopt the *GW*PT method[31], which provides a more precise description going beyond the

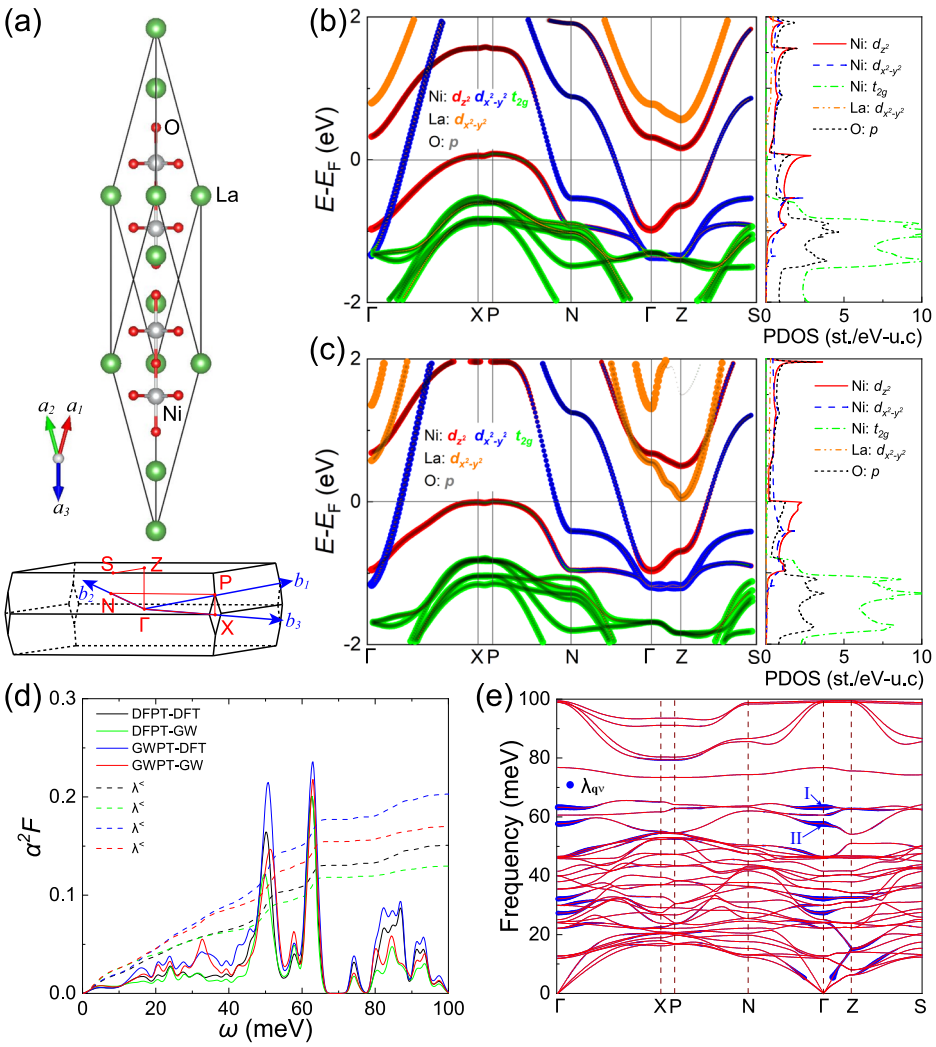

Fig. 1 | GW self-energy effects in electronic structure and electron-phonon coupling. **a** Primitive unit cell of $La_3Ni_2O_7$ in the *I*4/*mmm* structure and its corresponding Brillouin zone with high-symmetry **k**-points labeled. **b**, **c** Band structure of $La_3Ni_2O_7$ (at 30 GPa) at the DFT and *GW* levels, along with the projected density of states, respectively. **d** Eliashberg function and cumulative *e*-ph coupling strength $\lambda^<(\omega) = 2\int_0^{\omega}\frac{\alpha^2F(\omega')}{\omega'}d\omega'$ as a function of phonon frequency, calculated with DFPT or *GW*PT *e*-ph matrix elements and with the DFT or *GW* band structures, respectively. **e** Phonon band structure with phonon mode-decomposed *e*-ph coupling strength $\lambda_{\mathbf{q}\nu}$ (at the full *GW* level), where two A_{1g} modes at the Γ point are labeled as I and II.

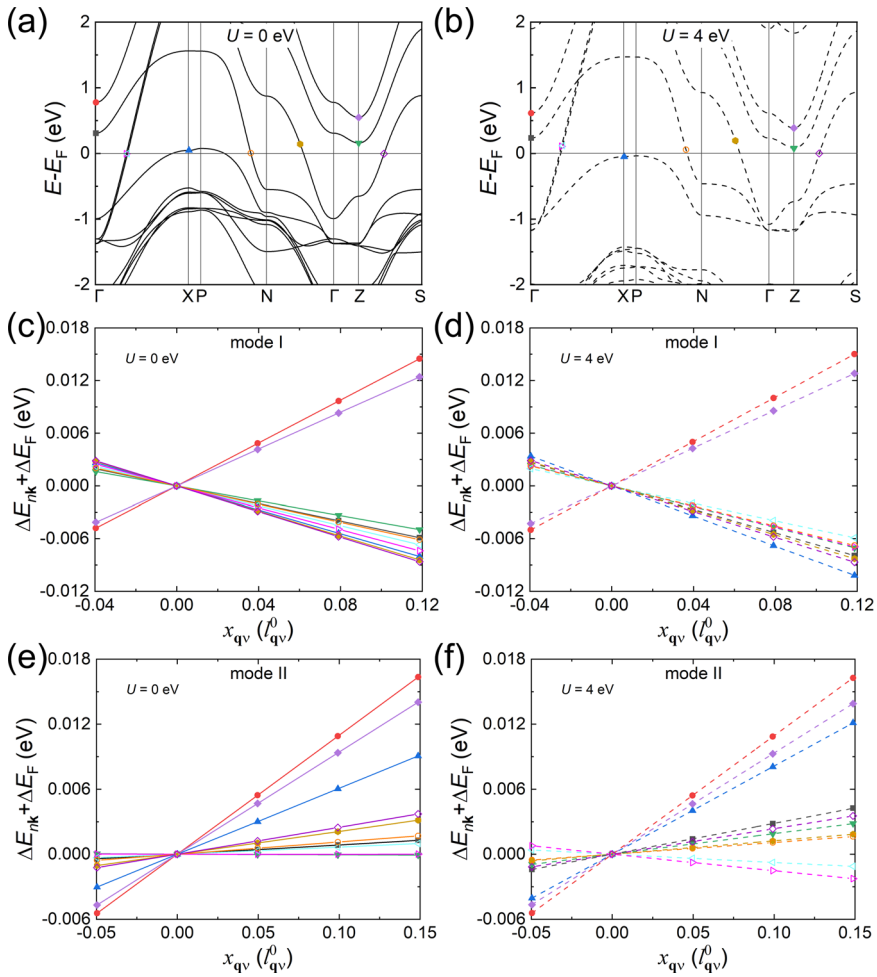

Fig. 2 | DFT+*U* and frozen-phonon calculations. Comparison of DFT band structures **a** without and **b** with Hubbard *U*. Color dots represent relevant states near E_F for further analysis. **c–f** Band energy shifts for the corresponding selected states in (**a**) and (**b**) as a function of atom displacements $x_{\mathbf{q}\nu}$ following the vibration modes I and II, respectively. The frozen-phonon displacements are in unit of the zero-point displacement $l^0_{\mathbf{q}\nu} = \sqrt{\hbar/2M_0\omega_{\mathbf{q}\nu}}$ (M_0 is set as the proton mass)[46], which take on values of 0.3422 and 0.3585 Bohr for modes I and II, respectively.

standard density-functional perturbation theory[45,46] (DFPT). General *e*-ph properties of materials can be microscopically constructed[46] using electron band energies (from DFT or *GW*) and *e*-ph matrix elements (from DFPT or *GW*PT). Figure 1d shows the Eliashberg spectral functions $\alpha^2F(\omega)$ and cumulative *e*-ph coupling strength $\lambda^<(\omega)$ using different combinations of approaches. We note that *GW*PT enhances the *e*-ph coupling by ~30% compared to DFPT (both using the same band structure) through renormalization in the *e*-ph matrix elements, but the *GW* band structure weakens the overall coupling strength compared to that with the DFT band structure (both using the same *e*-ph matrix elements), due to the reduction of the total density of states near E_F from 4.48 to 2.03 states/eV-unit-cell. The *GW* self-energy effects on the band structure and the *e*-ph matrix elements have a cancellation effect, leading to a similar *e*-ph coupling constant λ to the DFT and DFPT results. Nevertheless, the λ with or without the *GW* self-energy effects remains small as $\lambda \lesssim 0.2$. The Eliashberg functions reveal that the main coupling modes are around 50 and 63 meV, corresponding to the *e*-ph interactions that are more spread out in the Brillouin zone and localized near Γ at the corresponding frequencies, respectively, as shown by the phonon mode-decomposed *e*-ph coupling strength $\lambda_{\mathbf{q}\nu}$ ($\mathbf{q}\nu$: phonon wave vector and branch index) in Fig. 1e.

Local Hubbard *U* effects

While the *GW* approximation captures important long-range, non-local, and frequency-dependent correlation effects, local correlation effects (such as those drive Mott insulating phases) are typically not well contained in the *GW* diagrammatic expansion of the self-energy[47]. To address local correlation effects on the *e*-ph coupling, we adopt a DFT+*U* approach (with $U = 4$ eV on Ni 3*d* orbitals) combined with the frozen-phonon technique[43]. (A linear-response DFPT+*U* approach[48] can provide a more systematic study, as *GW*PT.) We first compare the electron band structures both without and with *U*, as depicted in Fig. 2a and b. While Hubbard *U* shows minimal influence on the electronic states near E_F, it induces a dramatic energy splitting between the t_{2g} and e_g orbitals. The *e*-ph coupling information can be extracted using a frozen-phonon approach, where atoms are displaced following specific phonon eigenmodes. We focus on two strongly coupled zone-center A_{1g} modes ~60 meV, labeled as mode I and II in Fig. 1e. The intraband coupling for ten states (denoted by dots in Fig. 2a and b) is analyzed by tracking their band energy shifts $\Delta E_{n\mathbf{k}}$ ($n\mathbf{k}$: electron band index and wave vector) with respect to the phonon mode displacement $x_{\mathbf{q}\nu}$ for mode I and II. Here, the band energy $E_{n\mathbf{k}}$ is defined relative to E_F. The intraband *e*-ph matrix elements can be directly mapped from the band energy shift for $\mathbf{q} = \Gamma$ phonon mode, with frozen-phonon displacements defined within a single unit cell (see Supplementary Fig. 1). In Fig. 2c–f, we plot $\Delta E_{n\mathbf{k}} + \Delta E_F$ as a function of the phonon-mode displacement[46] $x_{\mathbf{q}\nu}$, where the slope corresponds to the intraband *e*-ph matrix element, i.e., $g_{nn\nu}(\mathbf{k}, \mathbf{q} = \Gamma)$ in the linear-response limit (see Methods). Comparing Fig. 2c *vs* d, and Fig. 2e *vs* f, we observe that the Hubbard *U* only moderately modifies the overall *e*-ph interactions (represented by the slopes of corresponding states). The maximal enhancement of the *e*-ph coupling matrix elements for *strong* coupling modes within this subset of states by Hubbard *U* is less than 45% (green dot for mode I: ~42%, blue dot for mode II: ~34%). Assuming a uniform renormalization of all *e*-ph matrix elements by Hubbard *U* to a similar degree (i.e., of ~40% enhancement in $|g|$, which sets an upper bound as most elements are only slightly renormalized), the overall *e*-ph coupling strength can be enhanced by roughly a factor of ~2 (since $\lambda \sim |g|^2$). Nevertheless, the *e*-ph coupling constant λ remains in the weak-

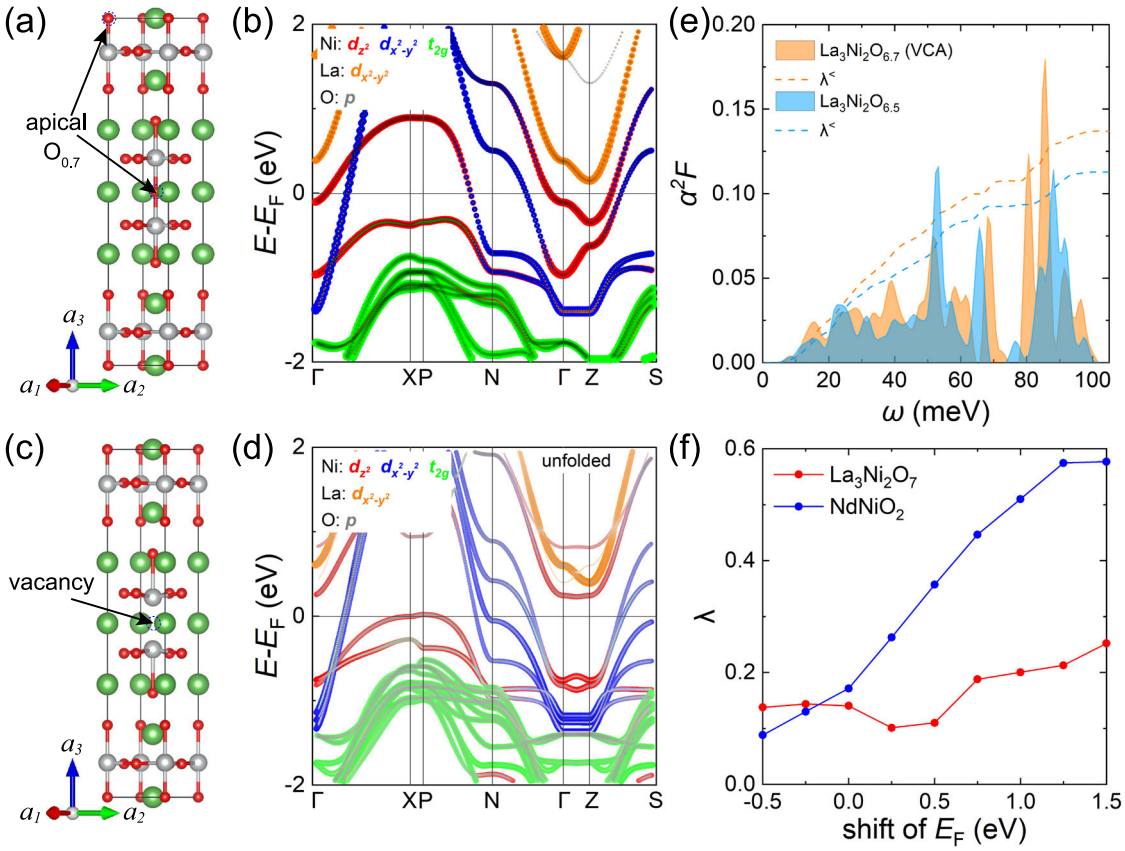

Fig. 3 | Doping effects. **a** Crystal structure of $La_3Ni_2O_{7-\delta}$ ($\delta = 0.3$), with each inner apical oxygen site 70%-occupied through VCA. **b** Electron band structure of $La_3Ni_2O_{6.7}$ at 30 GPa. **c** Crystal structure of $La_3Ni_2O_{6.5}$ with an explicit apical oxygen vacancy in the unit cell, and **d** its corresponding unfolded electron band structure. **e** The Eliashberg function $\alpha^2F(\omega)$ and the cumulative *e*-ph coupling $\lambda^<$ for $La_3Ni_2O_{6.7}$ (using VCA) and $La_3Ni_2O_{6.5}$ (with explicit vacancy). **f** The *e*-ph coupling strength λ *vs* the shift of E_F for $La_3Ni_2O_7$ and infinite-layer $NdNiO_2$ (see band structure in Supplementary Fig. 3).

coupling regime, between 0.3 and 0.5, significantly small to account for a strong-coupling scenario with $T_c \sim 80$ K.

Doping effects

After discussing the many-body and Coulomb interaction effects on the *e*-ph coupling, it is crucial to explore whether other realistic experimental conditions (besides pressure) alter the weak *e*-ph coupling picture. Oxygen vacancies, a prevalent form of intrinsic defects in $La_3Ni_2O_7$, have been directly visualized with predominant existence at the inner apical sites using energy-filtered multislice electron ptychography microscopy technique[49]. Here, we first adopt virtual crystal approximation[50] (VCA) by mixing pseudopotentials of O and Ne (at the apical oxygen sites) to simulate the (averaging) chemical environment of $La_3Ni_2O_{7-\delta}$ with $\delta = 0.3$ (Fig. 3a). This concentration of oxygen defects is close to the maximum level observed experimentally ($\delta \sim 0.34$)[49]. These vacancies introduce electron doping, leading to an effective downward shift of energy bands near the X and Z points by ~0.4−0.5 eV (Fig. 3b). Although the phonon band structure of $La_3Ni_2O_{6.7}$ closely resembles that of the pristine crystal (see Supplementary Fig. 2), stronger peaks emerge in the Eliashberg function $\alpha^2F(\omega)$ above 80 meV (Fig. 3e). However, the total *e*-ph coupling strength λ shows a marginal increase compared to the undoped phase (Fig. 1d). Since VCA does not capture possible local structural effects caused by O vacancies, we further analyze $La_3Ni_2O_{6.5}$ with explicit oxygen vacancies, as shown in Fig. 3c. In this case, both the Ni d_{z^2} and $d_{x^2-y^2}$ orbitals experience band splittings due to the altered octahedral environment, but the *e*-ph coupling constant λ becomes even smaller (Fig. 3e). Thus, it is unlikely that the high-T_c superconductivity in $La_3Ni_2O_7$ arises from *e*-ph coupling shaped by oxygen defects and electron doping effects.

In infinite-layer $Nd_{1-x}Sr_xNiO_2$, the *GW* self-energy largely enhances the DOS at the E_F from the rare-earth Nd d_{z^2} orbital and an interstitial orbital, contributing to strong *e*-ph coupling strength[27]. Here for $La_3Ni_2O_7$, we observe similar rare-earth band renormalization due to *GW* self-energy effects (see Fig. 1c), however, without a major enhancement in *e*-ph coupling. To understand the distinctive behaviors of the two nickelate superconductors, we perform a *numerical experiment* by rigidly shifting E_F upwards to recalculate the *e*-ph coupling constant λ (a Fermi surface property) of electron states at higher energies (Fig. 3f), which can potentially occur in real materials due to *GW* self-energy renormalization and/or electron doping. It becomes evident that the infinite-layer nickelate $Nd_{1-x}Sr_xNiO_2$ and Ruddlesden-Popper nickelate $La_3Ni_2O_7$ show completely different *e*-ph coupling landscapes. In $Nd_{1-x}Sr_xNiO_2$, the higher-energy Nd and interstitial states[27] (see band structure in Supplementary Fig. 3) already present strong *e*-ph coupling at the DFT level, which is further amplified at E_F after applying the *GW* and *GW*PT corrections[27]. However, higher energy states in $La_3Ni_2O_7$, including La $d_{x^2-y^2}$ orbitals, host only weak *e*-ph coupling, in strong contrast to $Nd_{1-x}Sr_xNiO_2$ (Fig. 3f). The distinction is even more striking given that the superconducting T_c is much higher in $La_3Ni_2O_7$ (~80 K) than in $Nd_{1-x}Sr_xNiO_2$ (~20 K), disfavoring an *e*-ph mediated pairing mechanism in $La_3Ni_2O_7$. In addition, we explore the effect of shifting the E_F downwards, accounting for potential upward shifts of the Ni-d_{z^2} band due to other effects not explored in this work. As shown in Fig. 3f, the λ of $La_3Ni_2O_7$ remains largely unaffected by this downward shift of the E_F, further suggesting that the *e*-ph coupling within the Ni-d_{z^2} band is also too weak to mediate the observed superconductivity. Further downward shift of the E_F would intersect with the Ni-t_{2g} band manifold, leading to unrealistic modifications of the electronic structure near E_F.

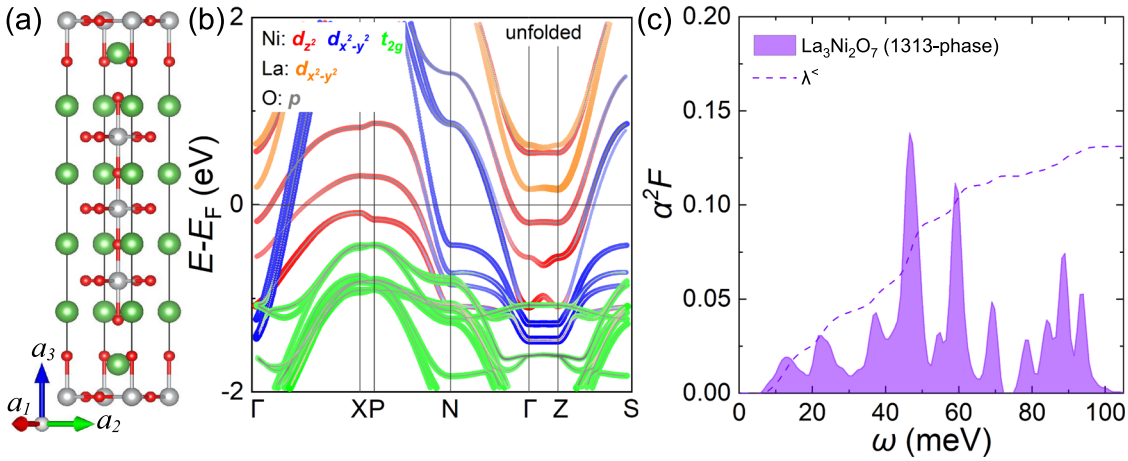

Fig. 4 | Alternative structural phase. a Crystal structure of $La_3Ni_2O_7$ with the *P*4/*mmm* unit cell at high pressure, with alternating single- and trilayer motifs. **b** The unfolded electron band structure, and **c** the Eliashberg function $\alpha^2F(\omega)$ and the cumulative *e*-ph coupling $\lambda^<(\omega)$.

Different structural phases

The *I*4/*mmm* structure we have investigated so far consists of two adjacent Ni-O layers (denoted as LNO-2222). Recent experiments have unveiled another possible structural phase of $La_3Ni_2O_7$ that contains alternating monolayer and trilayer units of NiO_6 octahedra[51–53] (denoted as LNO-1313) as shown in Fig. 4a. It is essential to assess the *e*-ph coupling strength in this alternative structural phase as well. Similar to the electronic structure of LNO-2222 (Fig. 1b), LNO-1313 with *P*4/*mmm* space group[52] predominantly presents Ni $d_{x^2-y^2}$ and d_{z^2} characters near E_F (Fig. 4b). The alternating NiO_6 octahedra induce an energy splitting of the Ni 3*d* subbands. Despite the distinct layer stacking order in LNO-1313, the phonon characteristics and *e*-ph coupling (Fig. 4c) are similar to those of LNO-2222, with an *e*-ph coupling constant $\lambda = 0.13$, comparable to the weak coupling in the bilayer structure ($\lambda = 0.15$). Direct comparisons among the band structures defined in consistent Brillouin zones of the different structural phases are summarized in Supplementary Fig. S4. Last but not least, the *Cmcm* (*Amam*) structure phase of $La_3Ni_2O_7$ at ambient pressure also shows a small $\lambda = 0.2$ (see Supplementary Fig. 5), corroborating a consistent weak *e*-ph coupling scenario.

Discussion

Through our comprehensive studies, we have revealed rich insights into the *e*-ph interaction in $La_3Ni_2O_7$. Besides the key conclusion that *e*-ph coupling is highly unlikely to mediate superconductivity in Ruddlesden-Popper nickelates, our calculations reveal intriguing and nontrivial self-energy effects both in band structures (reordering of bands with different characters) and in *e*-ph matrix elements (enhancement effects), as well as the impact of local Hubbard *U* and different structural phases. By examining the *e*-ph coupling strength in states near E_F, we unravel the fundamental distinction in the *e*-ph interaction landscape compared to infinite-layer nickelates $Nd_{1-x}Sr_xNiO_2$, which have been predicted to be phonon-mediated superconductors[27]. We emphasize that the use of advanced first-principles approaches (such as *GW* and *GW*PT) is crucial for reaching robust conclusions, as growing evidence has pointed out the inadequate description of exchange-correlation effects for *e*-ph coupling in standard static DFT approaches, especially in oxides[30,31,41–44]. Our considerations of the various aspects on *e*-ph coupling, including the potential impact from many-electron correlations, provide a strong and conclusive perspective on the limited role of *e*-ph coupling in $La_3Ni_2O_7$.

Our results hence suggest that the high-T_c superconductivity in $La_3Ni_2O_7$ under high pressure is more likely driven by unconventional mechanisms. One plausible cause are spin fluctuations that are often linked to high-T_c superconductivity in strongly correlated materials, such as cuprates and iron-based superconductors[54]. In $La_3Ni_2O_7$, the presence of Ni-3*d* electrons may lead to magnetic interactions, potentially giving rise to spin fluctuations that mediate Cooper pairing[8,15,55–59]. In addition, orbital-selective correlations in the presence of different Ni-3*d* orbitals components could play a role[8,15,19,21]. Another possible mechanism is the charge ordering, which may result in an unconventional pairing[60–63]. The different proposed scenarios suggest that $La_3Ni_2O_7$ likely harbors a complex interaction phase space where electronic correlations[18,64,65], magnetism[55–58], and lattice dynamics[1,40,66] corroborate or compete with each other[67,68]. Further experimental and theoretical studies are necessary to elucidate these potential mechanisms and to reveal the origin of superconductivity in $La_3Ni_2O_7$.

In summary, we have thoroughly investigated the potential impact from *e*-ph coupling on the superconductivity in $La_3Ni_2O_7$ under pressure. Effects from electron correlations, oxygen vacancy, doping, and different structural phases, lead to only limited changes (including enhancements) on the weak *e*-ph coupling strength with $\lambda \lesssim 0.5$, too small to account for the experimentally reported $T_c \sim 80$ K[1]. Our work provides an in-depth understanding of the overall *e*-ph interaction landscape in $La_3Ni_2O_7$, strongly suggesting alternative (unconventional) mechanisms for explaining its high-T_c superconductivity, disfavoring a phonon-mediated, or at minimum, a phonon-alone-mediated pairing mechanism.

Methods

DFPT and *GW*PT calculations

This work contains several major computational steps, including density functional theory (DFT) and density-functional perturbation theory (DFPT) calculations performed using the ABINIT code[69] (unless otherwise stated), many-body perturbation theory with the *GW* and *GW* perturbation theory (*GW*PT) methods using the BerkeleyGW code[27,34,70], and electron-phonon coupling property calculations using the EPW code[71,72]. These steps are incorporated into a dedicated workflow[27].

In the DFT and DFPT calculations, we employ norm-conserving pseudopotentials[73,74] within the generalized gradient approximation for the exchange-correlation functional[75], and a plane-wave basis with a cutoff of 80 Ry for wavefunctions. The atomic coordinates are fully optimized by minimizing the forces on each of the 12 atoms at 30 GPa. Subsequently, DFT calculations (with a **k**-grid set to $16 \times 16 \times 16$) and DFPT calculations (with both **k**- and **q**-grids set to $4 \times 4 \times 4$) are performed to determine the ground-state properties and the linear-response changes due to atom displacements (36 patterns) at each **q**-point, respectively.

The *GW*PT calculation is performed with a screened Coulomb interaction cutoff of 25 Ry and a bare Coulomb interaction cutoff of 80 Ry using the BerkeleyGW code[27,70]. The inverse dielectric matrix $\epsilon^{-1}_{\mathbf{GG}'}(\mathbf{p})$ (where $\mathbf{G}'$s are the reciprocal lattice vectors), and the linear-response changes in the self-energy $\partial_{\mathbf{q}\nu}\Sigma^{e-e}(\mathbf{r},\mathbf{r}';\varepsilon)$ are constructed with 500 bands and a $4 \times 4 \times 4$ internal **p** grid[27].

The *e*-ph matrix elements $g^{\mathrm{DFT}}_{mn\nu}(\mathbf{k},\mathbf{q})$ and $g^{GW}_{mn\nu}(\mathbf{k},\mathbf{q})$ from DFPT and *GW*PT, respectively, are directly computed on coarse $4 \times 4 \times 4$ **k**- and

q-grids, and then interpolated using a Wannier function approach[76,77] with the EPW code[71]. Consistency in the gauge of the wavefunctions and matrix elements is crucial and is ensured throughout the entire procedure, including the DFT, DFPT, *GW*PT, and Wannier interpolation procedures[27]. The Wannier subspace contains 46 Wannier orbitals, with the initial projections set as the five *d* orbitals of each of the three La and two Ni atoms and three *p* orbitals of each of the seven O atoms. The *e*-ph coupling constant λ is calculated on the fine interpolated 24 × 24 × 24 **k**- and **q**-grids. All convergence parameters have been tested to ensure converged results.

The DFPT calculations directly compute all the *e*-ph matrix elements (with full m, n, ν, **k**, and **q** dependence) for the Wannier manifolds and beyond. However, due to the extremely demanding computational resources required by *GW*PT calculations, we compute a subset of *GW*PT matrix elements that contributes most dominantly to physical properties near E_F. In this work, our *GW*PT calculations directly compute, for all phonon branches, the matrix elements within the three bands (one d_{z^2} bonding state and two $d_{x^2-y^2}$ bands of Ni atoms) crossing E_F for all **k**- and **q**-points as well as those within 1 eV for **k**- and **q**-points of the d_{z^2} antibonding and La-$d_{x^2-y^2}$ states. Less relevant matrix elements (those away from E_F) take on their DFPT values in the subsequent EPW calculations.

The calculations for defective structures and LNO-1313 structure are conducted based on DFT and DFPT using the Quantum ESPRESSO package[78], with the same pseudopotentials[74]. The unfolded band structures (spectral functions) are obtained by projecting supercell states back to wave vectors in the primitive cell Brillouin zone[79,80]. The assessment of *e*-ph coupling constant as a function of the shift of the Fermi level for bulk $La_3Ni_2O_7$ and infinit-layer $NdNiO_2$ is carried out using the EPW code[71,72].

Frozen-phonon calculations

The two A_{1g} modes I and II are characterized dominantly by vibrations originating from outer apical and planar oxygen atoms. Mode I differs from mode II in the relative phase difference between the vibrations of the nearby outer apical oxygen atoms and planar oxygen atoms, as well as their vibrational amplitudes. The actual displacements can be determined from the mass-scaled phonon eigenvectors (see Supplementary Fig. 1).

As discussed in the main text, the frozen-phonon approach can directly relate certain *e*-ph matrix elements with the band energy shift for the zone-center (**q** = Γ) phonons. The correspondence is derived below. The band energy of unperturbed structure is denoted as,

$$E^0_{n\mathbf{k}} = \langle \psi^0_{n\mathbf{k}} | H^0 | \psi^0_{n\mathbf{k}} \rangle - E^0_F. \tag{1}$$

The frozen-phonon configuration (of a phonon mode $\mathbf{q}\nu$ with $\mathbf{q} = \Gamma$) introduces changes in both Hamiltonian and wavefunctions with some finite displacement $x_{\mathbf{q}\nu}$ in the mode basis, and thus the Hamiltonian diagonal matrix elements become (keeping up to first-order terms),

$$\begin{aligned} \langle \psi_{n\mathbf{k}} | H | \psi_{n\mathbf{k}} \rangle &= \langle \psi^0_{n\mathbf{k}} + \Delta\psi_{n\mathbf{k}} | H^0 + \Delta H | \psi^0_{n\mathbf{k}} + \Delta\psi_{n\mathbf{k}} \rangle \\ &\approx \langle \psi^0_{n\mathbf{k}} | H^0 | \psi^0_{n\mathbf{k}} \rangle + \langle \psi^0_{n\mathbf{k}} | \Delta H | \psi^0_{n\mathbf{k}} \rangle \\ &= \langle \psi^0_{n\mathbf{k}} | H^0 | \psi^0_{n\mathbf{k}} \rangle + g_{nn\nu}(\mathbf{k}, \mathbf{q} = \Gamma) \times x_{\mathbf{q}\nu}. \end{aligned} \tag{2}$$

The band energy shift can be written, to the first order, as,

$$\begin{aligned} \Delta E_{n\mathbf{k}} &= E_{n\mathbf{k}} - E^0_{n\mathbf{k}} \\ &= \langle \psi_{n\mathbf{k}} | H | \psi_{n\mathbf{k}} \rangle - E_F - \langle \psi^0_{n\mathbf{k}} | H^0 | \psi^0_{n\mathbf{k}} \rangle + E^0_F \\ &= g_{nn\nu}(\mathbf{k}, \mathbf{q} = \Gamma) \times x_{\mathbf{q}\nu} - \Delta E_F, \end{aligned} \tag{3}$$

and therefore,

$$g_{nn\nu}(\mathbf{k}, \mathbf{q} = \Gamma) = \frac{\Delta E_{n\mathbf{k}} + \Delta E_F}{x_{\mathbf{q}\nu}}. \tag{4}$$

Data availability

The datasets generated and analyzed during the current study are presented as figures and tables in the manuscript and Supplementary information, and are available from the corresponding author on reasonable request.

Code availability

Some codes used for this work are open-source, with the latest stable versions available at https://www.abinit.org for Abinit, http://www.wannier.org for Wannier90, https://berkeleygw.org for BerkeleyGW, https://www.quantum-espresso.org for Quantum Espresso, and https://docs.epw-code.org for EPW. Customized and internal versions of some of the above packages for specific functionalities may be made available upon reasonable request from the corresponding author.

Received: 12 June 2024; Accepted: 20 November 2024;
Published online: 06 January 2025

References

1. Sun, H. et al. Signatures of superconductivity near 80 K in a nickelate under high pressure. *Nature* **621**, 493–498 (2023).
2. Bednorz, J. G. & Muller, K. A. Possible high T_c superconductivity in the Ba–La–Cu–O system. *Z. Phys. B Condens. Matt.* **64**, 189–193 (1986).
3. Anderson, P. W. The resonating valence bond state in La_2CuO_4 and superconductivity. *Science* **235**, 1196–1198 (1987).
4. Lee, P. A., Nagaosa, N. & Wen, X.-G. Doping a Mott insulator: physics of high-temperature superconductivity. *Rev. Mod. Phys.* **78**, 17–85 (2006).
5. Keimer, B., Kivelson, S. A., Norman, M. R., Uchida, S. & Zaanen, J. From quantum matter to high-temperature superconductivity in copper oxides. *Nature* **518**, 179–186 (2015).
6. Luo, Z., Hu, X., Wang, M., Wú, W. & Yao, D.-X. Bilayer two-orbital model of $La_3Ni_2O_7$ under pressure. *Phys. Rev. Lett.* **131**, 126001 (2023).
7. Cao, Y. & Yang, Y.-f. Flat bands promoted by Hund's rule coupling in the candidate double-layer high-temperature superconductor $La_3Ni_2O_7$ under high pressure. *Phys. Rev. B* **109**, l081105 (2024).
8. Sakakibara, H., Kitamine, N., Ochi, M. & Kuroki, K. Possible high T_c superconductivity in $La_3Ni_2O_7$ under high pressure through manifestation of a nearly half-filled bilayer Hubbard model. *Phys. Rev. Lett.* **132**, 106002 (2024).
9. Gu, Y., Le, C., Yang, Z., Wu, X. & Hu, J. Effective model and pairing tendency in bilayer Ni-based superconductor $La_3Ni_2O_7$. Preprint at https://arxiv.org/abs/2306.07275 (2023).
10. Wú, W., Luo, Z., Yao, D.-X. & Wang, M. Superexchange and charge transfer in the nickelate superconductor $La_3Ni_2O_7$ under pressure. *Sci. China Phys. Mech. Astron.* **67**, 117402 (2024).
11. Shen, Y., Qin, M. & Zhang, G.-M. Effective bi-layer model Hamiltonian and density-matrix renormalization group study for the high-T_c superconductivity in $La_3Ni_2O_7$ under high pressure. *Chinese Phys. Lett.* **40**, 127401 (2023).
12. Yang, Y.-f., Zhang, G.-M. & Zhang, F.-C. Interlayer valence bonds and two-component theory for high-T_c superconductivity of $La_3Ni_2O_7$ under pressure. *Phys. Rev. B* **108**, l201108 (2023).
13. Wang, Y., Jiang, K., Wang, Z., Zhang, F.-C. & Hu, J. Electronic structure and superconductivity in bilayer $La_3Ni_2O_7$. Preprint at https://arxiv.org/html/2401.15097v1 (2024).
14. Yang, Q.-G., Wang, D. & Wang, Q.-H. Possible $s_{\pm}$-wave superconductivity in $La_3Ni_2O_7$. *Phys. Rev. B* **108**, l140505 (2023).
15. Liu, Y.-B., Mei, J.-W., Ye, F., Chen, W.-Q. & Yang, F. $s_{\pm}$-wave pairing and the destructive role of apical-oxygen deficiencies in $La_3Ni_2O_7$ under pressure. *Phys. Rev. Lett.* **131**, 236002 (2023).

16. Zhang, Y., Lin, L.-F., Moreo, A., Maier, T. A. & Dagotto, E. Structural phase transition, $s_{\pm}$-wave pairing, and magnetic stripe order in bilayered superconductor $La_3Ni_2O_7$ under pressure. *Nat. Commun.* **15**, 2470 (2024).
17. Oh, H. & Zhang, Y.-H. Type-II $t-j$ model and shared superexchange coupling from Hund's rule in superconducting $La_3Ni_2O_7$. *Phys. Rev. B* **108**, 174511 (2023).
18. Liao, Z. et al. Electron correlations and superconductivity in $La_3Ni_2O_7$ under pressure tuning. *Phys. Rev. B* **108**, 214522 (2023).
19. Lechermann, F., Gondolf, J., Bötzel, S. & Eremin, I. M. Electronic correlations and superconducting instability in $La_3Ni_2O_7$ under high pressure. *Phys. Rev. B* **108**, l201121 (2023).
20. Christiansson, V., Petocchi, F. & Werner, P. Correlated electronic structure of $La_3Ni_2O_7$ under pressure. *Phys. Rev. Lett.* **131**, 206501 (2023).
21. Qu, X.-Z. et al. Bilayer $t-J-J_{\perp}$ model and magnetically mediated pairing in the pressurized nickelate $La_3Ni_2O_7$. *Phys. Rev. Lett.* **132**, 036502 (2024).
22. Li, D. et al. Superconductivity in an infinite-layer nickelate. *Nature* **572**, 624–627 (2019).
23. Lee, K. et al. Linear-in-temperature resistivity for optimally superconducting (Nd,Sr)NiO_2. *Nature* **619**, 288–292 (2023).
24. Sakakibara, H. et al. Model construction and a possibility of cupratelike pairing in a new d^9 nickelate superconductor (Nd,Sr)NiO_2. *Phys. Rev. Lett.* **125**, 077003 (2020).
25. Wu, X. et al. Robust $d_{x^2-y^2}$-wave superconductivity of infinite-layer nickelates. *Phys. Rev. B* **101**, 060504 (2020).
26. Nomura, Y. & Arita, R. Superconductivity in infinite-layer nickelates. *Rep. Prog. Phys.* **85**, 052501 (2022).
27. Li, Z. & Louie, S. G. Two-gap superconductivity and the decisive role of rare-earth *d* electrons in infinite-layer nickelates. *Phys. Rev. Lett.* **133**, 126401 (2024).
28. Nomura, Y. et al. Formation of a two-dimensional single-component correlated electron system and band engineering in the nickelate superconductor $NdNiO_2$. *Phys. Rev. B* **100**, 205138 (2019).
29. Li, Z., Antonius, G., Chan, Y.-H. & Louie, S. G. Electron-phonon coupling from GW perturbation theory: practical workflow combining BerkeleyGW, ABINIT, and EPW. *Comput. Phys. Commun.* **295**, 109003 (2024).
30. Li, Z., Wu, M., Chan, Y.-H. & Louie, S. G. Unmasking the origin of kinks in the photoemission spectra of cuprate superconductors. *Phys. Rev. Lett.* **126**, 146401 (2021).
31. Li, Z., Antonius, G., Wu, M., da Jornada, F. H. & Louie, S. G. Electron-phonon coupling from ab initio linear-response theory within the *GW* method: correlation-enhanced interactions and superconductivity in $Ba_{1-x}K_xBiO_3$. *Phys. Rev. Lett.* **122**, 186402 (2019).
32. Hedin, L. New method for calculating the one-particle Green's function with application to the electron-gas problem. *Phys. Rev.* **139**, A796–A823 (1965).
33. Hedin, L. & Lundqvist, B. I. Explicit local exchange-correlation potentials. *J. Phys. C: Solid State Phys.* **4**, 2064 (1971).
34. Hybertsen, M. S. & Louie, S. G. Electron correlation in semiconductors and insulators: band gaps and quasiparticle energies. *Phys. Rev. B* **34**, 5390–5413 (1986).
35. Dudarev, S. L., Botton, G. A., Savrasov, S. Y., Humphreys, C. J. & Sutton, A. P. Electron-energy-loss spectra and the structural stability of nickel oxide: an LSDA+U study. *Phys. Rev. B* **57**, 1505–1509 (1998).
36. Liechtenstein, A. I., Anisimov, V. I. & Zaanen, J. Density-functional theory and strong interactions: orbital ordering in Mott-Hubbard insulators. *Phys. Rev. B* **52**, R5467–R5470 (1995).
37. Errea, I. et al. Quantum crystal structure in the 250-kelvin superconducting lanthanum hydride. *Nature* **578**, 66–69 (2020).
38. Duan, D. et al. Structure and superconductivity of hydrides at high pressures. *Natl. Sci. Rev.* **4**, 121–135 (2016).
39. Dolui, K. et al. Feasible route to high-temperature ambient-pressure hydride superconductivity. *Phys. Rev. Lett.* **132**, 166001 (2024).
40. Wang, L. et al. Structure responsible for the superconducting state in $La_3Ni_2O_7$ at high-pressure and low-temperature conditions. *J. Am. Chem. Soc.* **146**, 7506–7514 (2024).
41. Lazzeri, M., Attaccalite, C., Wirtz, L. & Mauri, F. Impact of the electron-electron correlation on phonon dispersion: failure of LDA and GGA DFT functionals in graphene and graphite. *Phys. Rev. B* **78**, 081406 (2008).
42. Faber, C., Janssen, J. L., Côté, M., Runge, E. & Blase, X. Electron-phonon coupling in the C_{60} fullerene within the many-body *GW* approach. *Phys. Rev. B* **84**, 155104 (2011).
43. Yin, Z. P., Kutepov, A. & Kotliar, G. Correlation-enhanced electron-phonon coupling: applications of *GW* and screened hybrid functional to bismuthates, chloronitrides, and other high-T_c superconductors. *Phys. Rev. X* **3**, 021011 (2013).
44. Antonius, G., Poncé, S., Boulanger, P., Côté, M. & Gonze, X. Many-body effects on the zero-point renormalization of the band structure. *Phys. Rev. Lett.* **112**, 215501 (2014).
45. Baroni, S., de Gironcoli, S., Dal Corso, A. & Giannozzi, P. Phonons and related crystal properties from density-functional perturbation theory. *Rev. Mod. Phys.* **73**, 515–562 (2001).
46. Giustino, F. Electron-phonon interactions from first principles. *Rev. Mod. Phys.* **89**, 015003 (2017).
47. Wu, M., Li, Z., Cao, T. & Louie, S. G. Physical origin of giant excitonic and magneto-optical responses in two-dimensional ferromagnetic insulators. *Nat. Commun.* **10**, 2371 (2019).
48. Zhou, J.-J. et al. Ab initio electron-phonon interactions in correlated electron systems. *Phys. Rev. Lett.* **127**, 126404 (2021).
49. Dong, Z. et al. Visualization of oxygen vacancies and self-doped ligand holes in $La_3Ni_2O_{7-\delta}$. *Nature* **630**, 847–852 (2024).
50. Ghosez, P., Desquesnes, D., Gonze, X. & Rabe, K. M. First-principles study of lattice instabilities in $Ba_xSr_{1-x}TiO_3$. *AIP Conference Proceedings* **535**, 102–110 (2000).
51. Wang, H., Chen, L., Rutherford, A., Zhou, H. & Xie, W. Long-range structural order in a hidden phase of Ruddlesden–Popper bilayer nickelate $La_3Ni_2O_7$. *Inorg. Chem.* **63**, 5020–5026 (2024).
52. Puphal, P. et al. Unconventional crystal structure of the high-pressure superconductor $La_3Ni_2O_7$. *Phys. Rev. Lett.* **133**, 146002 (2024).
53. Chen, X. et al. Polymorphism in the Ruddlesden–Popper nickelate $La_3Ni_2O_7$: discovery of a hidden phase with distinctive layer stacking. *J. Am. Chem. Soc.* **146**, 3640–3645 (2024).
54. Scalapino, D. J. A common thread: the pairing interaction for unconventional superconductors. *Rev. Mod. Phys.* **84**, 1383–1417 (2012).
55. Chen, K. et al. Evidence of spin density waves in $La_3Ni_2O_{7-\delta}$. *Phys. Rev. Lett.* **132**, 256503 (2024).
56. Chen, X. Electronic and magnetic excitations in $La_3Ni_2O_7$. *Nat. Commun.* **15**, 9597 (2024).
57. Xie, T. et al. Strong interlayer magnetic exchange coupling in La_3Ni_2O7-$_\delta$ revealed by inelastic neutron scattering. *Science Bulletin* **69**, 3221 (2024).
58. Dan, Z. et al. Spin-density-wave transition in double-layer nickelate $La_3Ni_2O_7$. Preprint at https://arxiv.org/abs/2402.03952 (2024).
59. Heier, G., Park, K. & Savrasov, S. Y. Competing d_{xy} and $s_{\pm}$ pairing symmetries in superconducting $La_3Ni_2O_7$: LDA + FLEX calculations. *Phys. Rev. B* **109**, 104508 (2024).
60. Zhang, Y. et al. High-temperature superconductivity with zero resistance and strange-metal behaviour in $La_3Ni_2O_{7-\delta}$. *Nat. Phys.* **20**, 1269–1273 (2024).
61. Wang, G. et al. Pressure-induced superconductivity in polycrystalline $La_3Ni_2O_{7-\delta}$. *Phys. Rev. X* **14**, 011040 (2024).
62. Khasanov, R. et al. Pressure-induced split of the density wave transitions in $La_3Ni_2O_{7-\delta}$. Preprint at https://arxiv.org/abs/2402.10485 (2024).

63. Meng, Y. et al. Density-wave-like gap evolution in La_3Ni_2O7 under high pressure revealed by ultrafast optical spectroscopy. *Nat. Commun.* **15**, 10408 (2024).
64. Yang, J. et al. Orbital-dependent electron correlation in double-layer nickelate $La_3Ni_2O_7$. *Nat. Commun.* **15**, 4373 (2024).
65. Liu, Z. et al. Electronic correlations and partial gap in the bilayer nickelate $La_3Ni_2O_7$. *Nat. Commun.* **15**, 7570 (2024).
66. Li, Y. et al. Distinct ultrafast dynamics of bilayer and trilayer nickelate superconductors regarding the density-wave-like transitions. *Science Bulletin*, published online, https://doi.org/10.1016/j.scib.2024.10.011.
67. Yi, X.-W. et al. Nature of charge density waves and metal-insulator transition in pressurized $La_3Ni_2O_7$. *Phys. Rev. B* **110**, L140508 (2024).
68. Ouyang, Z., Gao, M. & Lu, Z.-Y. Absence of electron-phonon coupling superconductivity in the bilayer phase of $La_3Ni_2O_7$ under pressure.*npj Quantum Materials* **9**, 80 (2024).
69. Gonze, X. et al. ABINIT: first-principles approach to material and nanosystem properties. *Comput. Phys. Commun.* **180**, 2582–2615 (2009).
70. Deslippe, J. et al. BerkeleyGW: a massively parallel computer package for the calculation of the quasiparticle and optical properties of materials and nanostructures. *Comput. Phys. Commun.* **183**, 1269–1289 (2012).
71. Poncé, S., Margine, E., Verdi, C. & Giustino, F. Epw: Electron–phonon coupling, transport and superconducting properties using maximally localized Wannier functions. *Comput. Phys. Commun.* **209**, 116–133 (2016).
72. Giustino, F., Cohen, M. L. & Louie, S. G. Electron-phonon interaction using Wannier functions. *Phys. Rev. B* **76**, 165108 (2007).
73. Hamann, D. R. Erratum: Optimized norm-conserving Vanderbilt pseudopotentials [phys. rev. b 88, 085117 (2013)]. *Phys. Rev. B* **95**, 239906 (2017).
74. van Setten, M. et al. The PseudoDojo: Training and grading a 85 element optimized norm-conserving pseudopotential table. *Comput. Phys. Commun.* **226**, 39–54 (2018).
75. Perdew, J. P., Burke, K. & Ernzerhof, M. Generalized gradient approximation made simple. *Phys. Rev. Lett.* **77**, 3865–3868 (1996).
76. Souza, I., Marzari, N. & Vanderbilt, D. Maximally localized Wannier functions for entangled energy bands. *Phys. Rev. B* **65**, 035109 (2001).
77. Mostofi, A. A. et al. An updated version of wannier90: a tool for obtaining maximally-localised Wannier functions. *Comput. Phys. Commun.* **185**, 2309–2310 (2014).
78. Giannozzi, P. et al. Quantum espresso: a modular and open-source software project for quantum simulations of materials. *J. Phys.: Condens. Matter* **21**, 395502 (2009).
79. Popescu, V. & Zunger, A. Extracting E versus $\vec{k}$ effective band structure from supercell calculations on alloys and impurities. *Phys. Rev. B* **85**, 085201 (2012).
80. Pacilè, D. et al. Narrowing of d bands of FeCo layers intercalated under graphene. *Appl. Phys. Lett.* **118**, 121602 (2021).

Acknowledgements

Funding for this project came from a cy pres award as part of the distribution of a settlement relating to fuel economy for gasoline-powered vehicles. We acknowledge the management of the seed funds by the Ershaghi Center for Energy Transition (E-CET) at the Viterbi School of Engineering, University of Southern California (USC). M.D.B. was supported by the Center for Computational Study of Excited-State Phenomena in Energy Materials (C2SEPEM) at Lawrence Berkeley National Laboratory (LBNL), which is funded by the U.S. Department of Energy (DOE), Office of Science, Basic Energy Sciences, Materials Sciences and Engineering Division under Contract No. DE-AC02-05CH11231, as part of the Computational Materials Sciences Program. J.Y.Y. and W.C. were supported by the Singapore National Research Foundation Investigatorship Program under Grant No. NRFI08-2022-0009. Advanced codes were provided by C2SEPEM at LBNL. An award for computer time was provided by the U.S. DOE's Innovative and Novel Computational Impact on Theory and Experiment (INCITE) Program. Computational resources were provided by Frontier at the Oak Ridge Leadership Computing Facility, which is a DOE Office of Science User Facility supported under Contract No. DE-AC05-00OR22725, and were provided by Frontera at Texas Advanced Computing Center at The University of Texas at Austin, which is supported by National Science Foundation under Grant No. OAC-1818253.

Author contributions

Z.L. directed the research. J.Y.Y. performed the calculations. J.Y.Y. and Z.L. wrote the manuscript. J.Y.Y., Z.Z., M.D.B., W.C., and Z.L. discussed the results and revised the manuscript.

Competing interests

The authors declare no competing interests.

Additional information

Supplementary information The online version contains supplementary material available at https://doi.org/10.1038/s41524-024-01483-4.

Correspondence and requests for materials should be addressed to Zhenglu Li.

Reprints and permissions information is available at http://www.nature.com/reprints

Publisher's note Springer Nature remains neutral with regard to jurisdictional claims in published maps and institutional affiliations.

Open Access This article is licensed under a Creative Commons Attribution-NonCommercial-NoDerivatives 4.0 International License, which permits any non-commercial use, sharing, distribution and reproduction in any medium or format, as long as you give appropriate credit to the original author(s) and the source, provide a link to the Creative Commons licence, and indicate if you modified the licensed material. You do not have permission under this licence to share adapted material derived from this article or parts of it. The images or other third party material in this article are included in the article's Creative Commons licence, unless indicated otherwise in a credit line to the material. If material is not included in the article's Creative Commons licence and your intended use is not permitted by statutory regulation or exceeds the permitted use, you will need to obtain permission directly from the copyright holder. To view a copy of this licence, visit http://creativecommons.org/licenses/by-nc-nd/4.0/.

© The Author(s) 2025